

High-Performance Shortwave-Infrared Light-Emitting Devices Using Core–Shell (PbS–CdS) Colloidal Quantum Dots

Geoffrey J. Supran,* Katherine W. Song, Gyu Weon Hwang, Raoul E. Correa, Jennifer Scherer, Eric A. Dauler, Yasuhiro Shirasaki, Mouni G. Bawendi, and Vladimir Bulović*

Shortwave-infrared light sources integrated at room temperature with any planar surface could be realized by harnessing the broad spectral tunability, high brightness, and solution-processability of colloidal quantum-dots (QDs).^[1] Yet the performance of shortwave-infrared quantum-dot light-emitting devices (QD-LEDs) has remained low compared with visible-emitting devices until now.^[1] Here we show that PbS–CdS core–shell QDs enhance the peak external quantum efficiency (EQE) of PbS core-only control devices by 50- to 100-fold, up to $4.3\% \pm 0.3\%$. “Turn-on” voltages are lowered by 0.6 ± 0.2 V and per-amp radiant intensities are increased by up to 150 times. Peak EQEs and power conversion efficiencies are more than double those of previous QD-LEDs^[2] emitting at wavelengths beyond 1 μm , and are comparable with those of commercial shortwave-infrared LEDs. We demonstrate that the primary origin of the performance enhancement is passivation of PbS cores by CdS shells against in situ photoluminescence (PL) quenching, suggesting that core–shell QDs may become a mainstay of high-efficiency shortwave-infrared QD-LEDs.

Electrically driven and wavelength-selectable near-infrared (NIR) and shortwave-infrared (SWIR) light sources that can be deposited on any substrate and at lower cost^[1] than existing (usually epitaxially grown) IR-emitters have the potential to enhance existing technologies and to trigger the development of new ones. Beneficiaries could include optical telecommunications and computing,^[3,4] biomedical imaging,^[4–6] on-chip bio(sensing) and spectroscopy,^[4,7,8] and night-time surveillance and other security applications. Among the candidate large-area planar light-emitting technologies, QD-LEDs^[1] and organic LEDs (OLEDs) stand out, as they enable room-temperature

processing and nonepitaxial deposition. Between them, QD-LEDs should perform better at wavelengths beyond $\lambda = 1$ μm because in this spectral range the luminescent organic dyes used in OLEDs exhibit lower photoluminescence quantum-yields ($\eta_{\text{PL}} < 5\%$)^[9] than the colloidal QDs used in QD-LEDs. The PL emission wavelength of QDs can be precisely tuned through quantum-confinement effects, with high η_{PL} maintained throughout the visible and SWIR ($\eta_{\text{PL}} > 95\%$ ^[10] and $\eta_{\text{PL}} > 50\%$, respectively, in solution). Furthermore, solution processability of QDs enables their epitaxy-free integration with Si-electronics.^[11] SWIR QD-LEDs with peak EQEs of 8.6% at $\lambda < 1$ μm ^[12] and 2% at $\lambda > 1$ μm ^[2] have so far been demonstrated, compared with 6.3%^[13] and $< 0.3\%$ ^[9] for OLEDs, respectively.

In this work, we significantly raise the performance of $\lambda > 1$ μm SWIR QD-LEDs by adopting strategies used in visible-emitting QD-LEDs (which have demonstrated EQEs of up to 20% in the red).^[14] One notable difference to date is that while visible-emitting QD-LEDs have employed core–shell QDs (QD cores overcoated by a wider bandgap inorganic shell) almost since their inception,^[15,16] SWIR QD-LEDs have, with one exception,^[17,18] been based solely on core-only QDs. The use of SWIR QDs without shells can compromise their intrinsic η_{PL} , increase their susceptibility to extrinsic PL quenching processes,^[19] and reduce their photostability.^[20] Second, the use of “type-IV QD-LED” (organic-QD-inorganic hybrid) architectures (as defined in our QD-LED review article),^[1] which have shown the highest EQEs, has heretofore been restricted almost exclusively to visible-emitting devices.^[1] Here we report a novel SWIR “type-IV QD-LED” and demonstrate that the use of core–shell PbS–CdS QDs results in an enhancement of peak EQEs of one to two orders of magnitude over PbS core-only controls. This is shown to be a consequence of increased in situ QD η_{PL} accrued by virtue of the passivating CdS shell. The peak EQEs and power conversion efficiencies obtained surpass those of any previously reported $\lambda > 1$ μm SWIR QD-LED.^[2]

Core-only (control) oleic-acid-capped PbS QDs were synthesized using the procedure described in the Experimental Section. The QDs were then subjected to a partial Pb^{2+} -to- Cd^{2+} cation-exchange reaction^[20] (Figure 1a and the Experimental Section), whereby the addition of a large excess of cadmium oleate yields core–shell PbS–CdS QDs, also capped with oleic acid. Growing wide bandgap shells such as CdS on PbS cores by cation-exchange likely circumvents mismatch of crystal structures encountered in traditional shell growth techniques.

The core-only PbS QDs have a mean diameter of 4.0 nm, deduced by transmission electron microscopy (TEM) and from the spectral position of the 1S excitonic absorption peak. This corresponds to a peak PL wavelength of $\lambda = 1315$ nm in solution. By

G. J. Supran, G. W. Hwang
Department of Materials Science and Engineering
Massachusetts Institute of Technology
Cambridge, MA 02139, USA
E-mail: gjsupran@mit.edu

K. W. Song, Dr. Y. Shirasaki, Prof. V. Bulović
Department of Electrical Engineering and Computer Science
Massachusetts Institute of Technology
Cambridge, MA 02139, USA
E-mail: bulovic@mit.edu

Dr. R. E. Correa, J. Scherer, Prof. M. G. Bawendi
Department of Chemistry
Massachusetts Institute of Technology
Cambridge, MA 02139, USA

Dr. E. A. Dauler
Lincoln Laboratory
Massachusetts Institute of Technology
Lexington, MA 02420, USA



DOI: 10.1002/adma.201404636

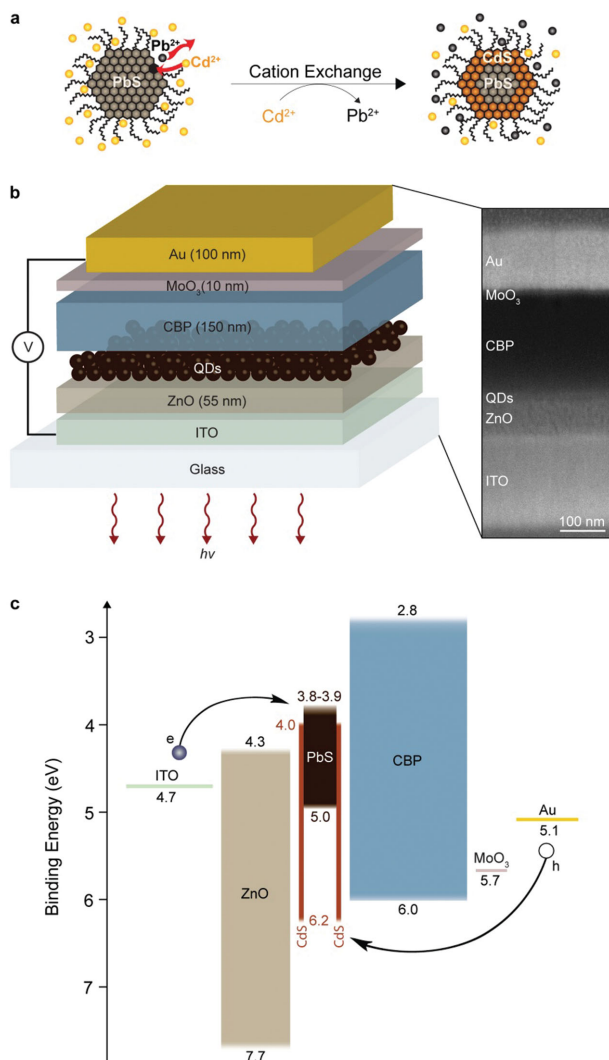


Figure 1. QD synthesis and QD-LED design. a) Schematic illustration of the cation-exchange reaction used to convert core-only PbS QDs into core-shell PbS-CdS QDs. b) Device architecture (left) and cross-sectional SEM image (right) of the “type-IV QD-LED” based on these QDs. c) The QD-LED’s flat-band energy level diagram. Band energies are in eV (referenced to the vacuum level) and are taken from literature.^[21,43–48] Based on the model in ref. [44], the electron affinity of PbS is tuned from approximately 3.8 to 3.9 eV by the reduction in core size (from 4.0 to 3.6 nm) accompanying cation-exchange.

cation-exchange we synthesized two types of thin-shelled PbS-CdS QDs and one type of thicker-shelled PbS-CdS QDs. The thin-shelled QDs have core diameters of 3.6 nm and shell thicknesses equivalent to 0.2 nm (assuming uniform shell coverage), but are distinguished by their synthesis injection temperatures of 80 °C (PbS-CdS (0.2 nm, Sample A)) and 100 °C (PbS-CdS (0.2 nm, Sample B)), respectively. The thicker-shelled PbS-CdS QDs have a core diameter of 2.6 nm and a shell thickness equivalent to 0.7 nm (PbS-CdS (0.7 nm)) (again assuming a uniform shell coverage). These dimensions were determined by wavelength dispersive spectroscopy (see the Experimental Section).

Using these QDs, we fabricated QD-LEDs comprising a zinc oxide (ZnO) sol-gel-derived, solution-processed electron-transport

layer (ETL), and an organic small molecule hole-transport layer (HTL) of 4,4-bis(carbazole-9-yl)biphenyl (CBP), sandwiching a film of QDs in an inverted “type-IV QD-LED” device architecture.^[1] Thin films of indium tin oxide (ITO), gold (Au), and molybdenum oxide (MoO_3) serve as cathode, anode, and hole-injection layers,^[21,22] respectively. A schematic diagram of the QD-LED and a scanning electron microscope (SEM) image of its cross-section are shown in Figure 1b. Its corresponding energy band-diagram is depicted in Figure 1c. As previous reports have shown,^[22] MoO_3 plays the vital role of mediating efficient hole-injection from the Au anode into the deep highest occupied molecular orbital (HOMO) of CBP.

Figure 2a presents EL spectra for these PbS and PbS-CdS QD-LEDs. Their overall agreement with corresponding PL spectra from the same locations confirms pure SWIR QD EL at a wavelength of $\approx 1.2 \mu\text{m}$. In the absence of a QD layer, high voltages (>4 V) induce low-intensity visible EL characterized by two peaks at $\lambda = 400$ nm and $\lambda = 670$ nm (see Figure 2a, inset), resulting from CBP and/or ZnO emission. However, upon addition of a QD layer, this parasitic emission is entirely suppressed, indicative of efficient carrier recombination solely within the QDs. Figure 2a shows that a blue-shift in EL and PL of more than 100 nm is achieved by adding a 0.7 nm CdS shell to core-only PbS. This is characteristic of increased exciton confinement due to a reduction in core size during cation-exchange.^[20] By fabricating similar devices with other batches of PbS and with thicker CdS shells, we have so far tuned EL peaks from PbS-CdS QDs between $\lambda = 1163$ nm and $\lambda = 1341$ nm. SWIR EL and current-dependent brightness is visualized with an infrared camera (Figure 2d, inset. A corresponding video is available in the Supporting Information).

The effect of shell growth on SWIR QD-LED performance is shown in Figure 2b–d, which compares core-only PbS QDs with PbS-CdS (0.2 nm, Sample B) QDs. Results for the other core-shell QDs are summarized in Figure 3b and Figure S1–S4, Supporting Information. Figure 2b shows that the current density–voltage (J – V) behavior for both core-only and overcoated QDs is described by $J \propto V^{m+1}$, a signature of trap-limited space-charge conduction.^[11,23] The corresponding radiance–voltage (L – V) plot (Figure 2c) shows that replacing the PbS QDs with PbS-CdS (0.2 nm, Sample B) QDs results in a reduction in “turn-on” voltage (measured at $3 \times 10^{-4} \text{ W sr}^{-1} \text{ m}^{-2}$) from 2.0 ± 0.1 to 1.4 ± 0.1 V. This may be due to more efficient QD charge injection, suggested by the simultaneous reduction in “turn-on” current density of more than an order of magnitude with increasing shell thickness^[16] (Figure S5, Supporting Information). Taken together, the J – V and L – V data yield an average peak power conversion efficiency of 2.4%; more than double that of any previous $\lambda > 1 \mu\text{m}$ SWIR QD-LED^[2] (Table S1, Supporting Information).

EQE-current density data are shown in Figure 2d. Core-shell PbS-CdS (0.2 nm, Sample B) QD-LEDs exhibit average peak EQEs of $4.3\% \pm 0.3\%$. To our knowledge, this surpasses that of any previously reported $\lambda > 1 \mu\text{m}$ SWIR QD-LED^[2] (Table S1 and Figure S6, Supporting Information). This EQE is also commensurate with those typical of commercial SWIR IR LEDs (from 3% to 12%),^[24] though at significantly lower emission powers. In comparison, the average peak EQE of control core-only PbS QD-LEDs is approximately from 50 to 100 times lower: $0.05\% \pm 0.01\%$; consistent with the performance of QD-LEDs previously

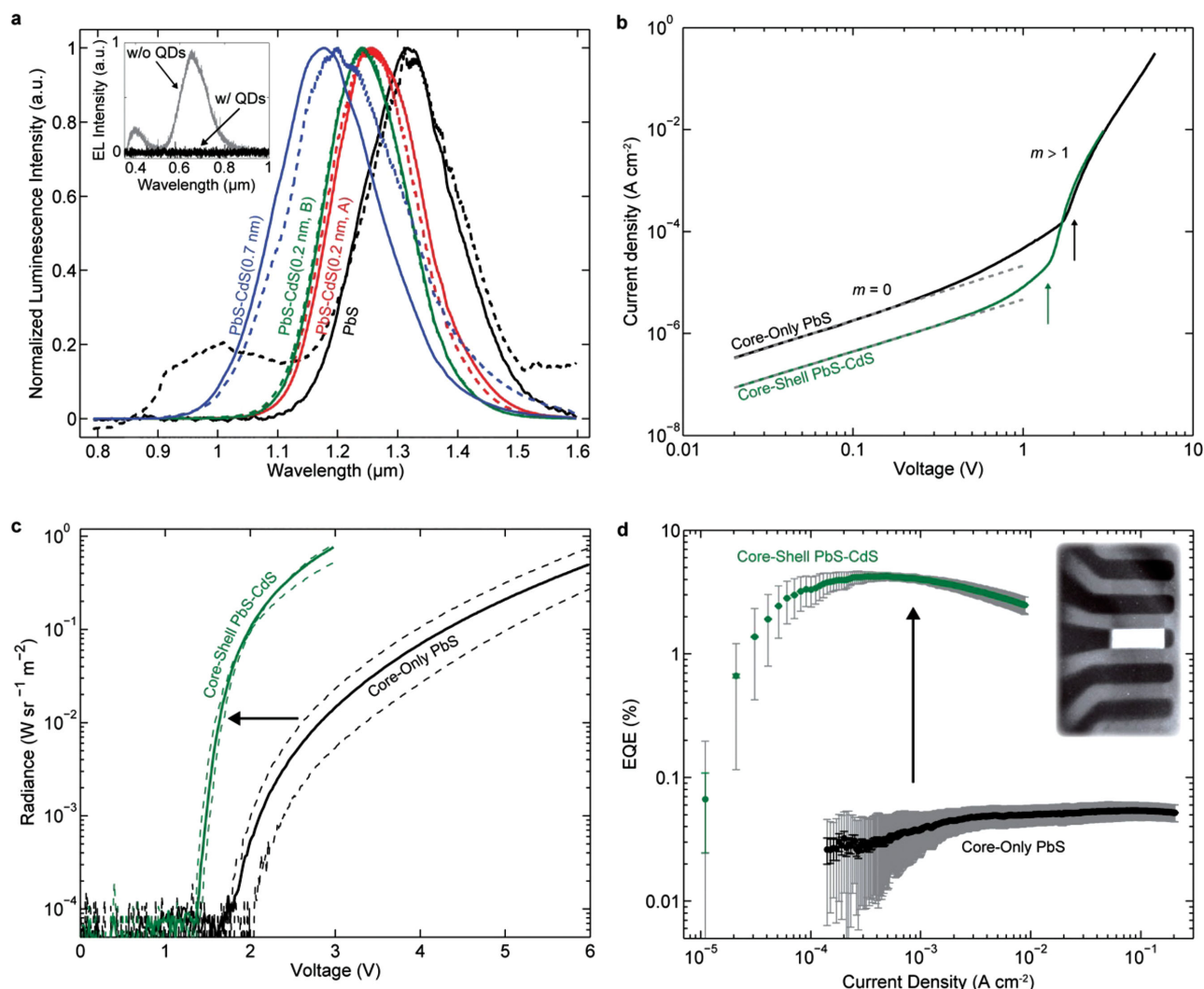


Figure 2. QD-LED performance using core-only versus core-shell QDs. a) Normalized electroluminescence (solid line, 3 V applied bias) and photoluminescence (dashed line) spectra of QD-LEDs containing (black) PbS; (red) PbS-CdS (0.2 nm, Sample A); (green) PbS-CdS (0.2 nm, Sample B); and (blue) PbS-CdS (0.7 nm) QDs. Inset: Normalized electroluminescence spectra of otherwise identical LEDs (with the structure shown in Figure 1) with and without a film of QDs (8 and 6 V applied biases, respectively). b) Average current density-voltage (J - V) behavior of: (black) core-only PbS; and (green) core-shell PbS-CdS (0.2 nm, Sample B) QD-LEDs. The dashed grey lines are fits to $J \propto V^{m+1}$, with $m = 0$ and $m > 1$ corresponding to Ohmic and trap-limited space-charge conduction regimes, respectively. The arrows indicate electroluminescence “turn-on,” which coincides with the upturn in slope of the J - V curves. c) Radiance-voltage characteristics of these devices. Solid lines represent average radiances and dotted lines correspond to minimum and maximum “turn-on” voltages recorded for all measured devices. Black and green error bars indicate experimental measurement errors while the standard deviation of device-to-device variations are shown in grey (Section A, Supporting Information). Inset: Photograph of an array of five QD-LEDs taken with an infrared camera, with the middle device turned on (active area of 1.21 mm^2) and emitting at a center wavelength of $\lambda = 1242 \text{ nm}$.

reported using core-only PbS with similar long-chain carboxylic acid ligands.^[2] As shown in Figure 3b (black columns), EQE is sizably enhanced for all core-shell QDs investigated. A direct consequence of this is that radiant intensity efficiencies (radiant intensity per amp) are increased at all current densities above “turn-on” by between 35 and 150 times by switching from core-only to core-shell QDs (Figures S5 and S7, Supporting Information). The grey columns in Figure 3b represents the average peak EQEs observed from an anomalous (not included in any averaged performance data) “champion” set of devices: up to $8.3\% \pm 1.0\%$ for PbS-CdS (0.2 nm, Sample B) QD-LEDs (Figure S8,

Supporting Information). Repeated measurements of these “champion” devices manifested persistently stable operation, suggesting that SWIR QD-LEDs with EQE > 10% may be within reach.

Since the EQE of a QD-LED is proportional to η_{PL} of its emitting QDs,^[1] we can better understand the dramatic increase in EQE that comes from replacing core-only QDs with core-shell QDs by quantifying the correlation between changes in EQE and in η_{PL} of the QDs in our devices. Even at zero-bias, η_{PL} can be subject to in situ PL quenching mechanisms^[1] such as exciton energy transfer to conductive charge-transport layers (CTLs),^[25–27] exciton dissociation at CTL/QD interfaces^[28–49] and Auger recombination.^[31]

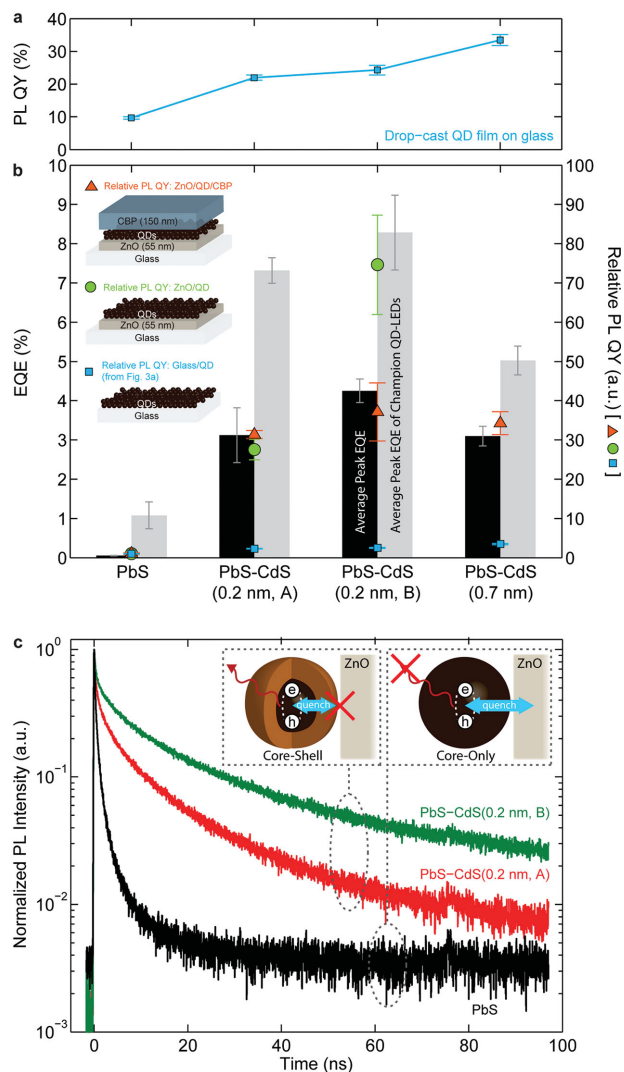


Figure 3. Correlation of QD-LED EQE with QD PL quantum yields. a) Absolute photoluminescence quantum yields (PL QYs) of drop-cast films of core-only (PbS) and core-shell (PbS–CdS) QDs on glass as a function of shell thickness, measured using an integrating sphere (described in the Experimental Section). Cation-exchange serves as a facile post-synthesis approach to increasing η_{PL} of SWIR-emitting QDs to unprecedented values (η_{PL} = 33% in thin-film for a 0.7 nm shell). Error bars show standard deviations of the values measured at four locations per sample. b) Corresponding dependence of QD-LED average peak EQE on QD shell thickness is indicated by black columns. These EQEs correlate well with average relative in situ η_{PL} of spin-cast films of these QDs (η_{PL} of core-only QDs is normalized to unity) in (green spots) glass/ZnO/QD; and (orange triangles) glass/ZnO/QD/CBP optical structures, depicted schematically in the inset. In contrast, relative intrinsic QD η_{PL} (blue squares), taken from a), greatly underestimate the EQE enhancements. Average peak EQEs obtained from a “champion” set of devices are shown as grey columns. The EQE error bars for the main devices (black columns) and the “champion” devices (grey columns) indicate device-to-device variations (see the Experimental Section and Section A, Supporting Information for details). The QD η_{PL} error bars show standard deviations between values measured at roughly five locations per sample. c) Normalized time-dependent PL intensity of spin-cast films of (black) PbS; (red) PbS–CdS (0.2 nm, Sample A); and (green) PbS–CdS (0.2 nm, Sample B) QDs, all on ZnO. Inset: Illustrations depicting the passivation of ZnO-induced PbS PL quenching (blue two-headed arrow) by CdS shells.

We therefore measure relative η_{PL} of each type of QD in glass/ZnO/QD/CBP and glass/ZnO/QD structures (Figure 3b, inset) that replicate the QDs’ in situ environment in our QD-LEDs. Relative η_{PL} is quantified by comparing the integrated areas under the steady-state PL spectra of the QDs in these structures (see the Experimental Section). The results for each type of QD are shown in Figure 3b relative to η_{PL} of core-only PbS, which has been normalized to unity. Whereas shell growth produces only a threefold rise in η_{PL} of QD-only (glass/QD) samples (blue in Figure 3a,b), relative η_{PL} of these QDs in situ (orange and green in Figure 3b) increase by 30 to 100 times, indicating that the CdS shell significantly passivates PbS QDs against in situ nonradiative pathways. The similarity of the results for test structures with and without CBP (orange versus green in Figure 3b) implies that ZnO is mostly responsible for the PL quenching. The generally good agreement between relative in situ η_{PL} and average peak EQE (black columns) indicates that the shell-induced increases in η_{PL} predominantly explain the efficiency enhancements achieved. This is further substantiated by the reproducibility of this correlation for EQE data corresponding to all measured current densities; examples at $\approx 10^{-4}$ A cm $^{-2}$ and $\approx 10^{-2}$ A cm $^{-2}$ are shown in Figure S9 in the Supporting Information.

Time-resolved PL spectroscopy offers further insights into the shell-dependent QD PL quenching by ZnO. Figure 3c shows the normalized transient QD PL decay curves for the glass/ZnO/QD samples. Compared with glass/QD samples (Figure S10, Supporting Information), PL lifetimes are reduced for all of the QD types in the presence of ZnO, indicative of PL quenching; similar changes have previously been seen for PbS QDs with other metal oxides.^[32] The longer PL lifetimes of core-shell versus core-only QDs (Table S2, Supporting Information) on ZnO corroborate our conclusion that the former are more effective at mitigating PL quenching.^[19,31–33]

What specific mechanisms, symbolized by the two-headed blue arrow in the inset of Figure 3c, underpin the ZnO-induced QD PL quenching in our devices? Non-radiative energy transfer from visibly colored QDs to surface plasmon modes in conductive metal oxide CTLs of QD-LEDs has previously been postulated,^[25] but is unlikely here given the low carrier density of our undoped ZnO.^[34,35] Indeed in general, energy transfer from PbS QDs to ZnO – for example, to ZnO midgap states – seems at odds with the very low extinction coefficients reported for sol-gel ZnO in the SWIR.^[34,36] Alternatively, electron transfer from PbS QDs to ZnO (which is widely observed in photovoltaics)^[28] or from ZnO to PbS (previously reported in red-emitting QD-LEDs)^[37] could be responsible. As has been noted in the context of CdSe–CdS QD quenching by ZnO nanocrystals,^[37,38] however, the energetic favourability of the ZnO/QD interface for electron transfer, in either direction, is expected to be voltage-dependent, whereas the ZnO-induced PL quenching that we observe is, at least in an order of magnitude, voltage-independent (Figure S9, Supporting Information). Hole transfer to ZnO midgap states^[38] is therefore more plausible, yet the challenge in reconciling either energy or charge transfer models with the extremely short length scales on which PL quenching occurs (≈ 0.2 nm of CdS shell) points to a second possibility; quenching by defect states arising from the oxidation of PbS QDs by ZnO. In the case of visible CdSe or

CdS QDs, which are much less susceptible to surface oxidation and the associated extrinsic decay pathway, intrinsic processes such as multicarrier Auger recombination – recently proposed for CdSe-CdS QD-LEDs^[37] – may instead be the dominant quenching mechanism mitigated by passivating shells.

The roles of the QD core-shell structure and of the “type-IV QD-LED” architecture are inextricably linked. While the former largely explains the enhancement in EQEs observed, the latter is probably central to their high absolute magnitudes. The “type-IV QD-LED” design is conducive to efficient carrier recombination because it allows the processes of charge-transport and light-emission to be decoupled. Strikingly, the only two previously reported SWIR QD-LEDs are not possessing a “type-I QD-LED” structure (a more rudimentary architecture in which QDs play dual roles of CTL and emission center^[1] have also been the highest performing.^[2,12] With the present demonstration we propose that together, cation-exchanged core-shell QDs, and a “type-IV QD-LED” device architecture offer a new paradigm for the design of high-efficiency SWIR QD-LEDs.

This work demonstrates that the efficiency of SWIR QD-LEDs can be enhanced by up to 100 times by replacing SWIR core-only QDs with core-shell QDs, as a result of a corresponding increase in in situ QD η_{PL} . As the demand for high brightness – and therefore high current density – QD-LEDs continues to necessitate the use of metal oxide charge-transport materials^[39] (that commonly quench QD PL), the use of core-shell QDs can serve as a general strategy by which to maximise the performance of future SWIR QD-LEDs.

Experimental Section

QD Synthesis and Characterization: Based on previously published procedures, core-only PbS QDs were synthesized using a large-scale method^[40] and core-shell PbS-CdS QDs were synthesized by cation-exchange^[20,41] (Section B, Supporting Information). QD shell thicknesses were deduced from elemental analysis of drop-cast films on glass substrates by wavelength dispersive spectroscopy.^[41]

QD-LED and Optical Sample Fabrication: Prior to device fabrication, the QDs undergo three rounds of precipitation and centrifugation with methanol and 1-butanol and are then re-dissolved in chloroform at 40 mg mL⁻¹ and filtered (0.45 μm PTFE). Devices are fabricated on glass substrates that are pre-patterned with a 150 nm thick film of indium-tin-oxide (ITO) (obtained from thin film devices) and cleaned with solvent and oxygen-plasma. First, a zinc acetate dihydrate solution (Section C, Supporting Information) is spin-cast onto the ITO at 2000 rpm for 30 s in a nitrogen-filled glovebox. The xerogel is then sintered on a hot-plate at 300 °C for 5 min in the 10–20% relative humidity environment of a glove-bag continuously flushed with dry air. This process results in the crystallization of 55 ± 1 nm (by optical ellipsometry (Gaertner Scientific)) thick ZnO films and mitigates the sensitivity of ZnO to variations in atmospheric conditions. QD films are then deposited by spin-coating ca. 40 μL of ca. 5 mg mL⁻¹ PbS (or PbS-CdS) QDs in chloroform at 1500 rpm for 60 s; film thicknesses of 8 ± 1 nm are obtained, as determined by thickness-concentration calibration curves measured by profilometer (Tencor P-16) (Section D, Supporting Information). This level of accuracy is necessary in order to allow the effect of shell thickness to be studied independently from the effects of QD film thickness. A 150 nm thick HTL of 4,4-bis(carbazole-9-yl)biphenyl (CBP) (purified before use via thermal gradient sublimation), a 10 nm thick hole-injection layer of molybdenum oxide (MoO₃) and a 100 nm thick Au anode (shadow masked) are then successively deposited via thermal evaporation at a rate of ≈ 0.1 nm s⁻¹ at a base pressure of 1×10^{-6} Torr.

Overlap of anode and cathode defines active area pixels of 1.21 mm². The glass/ZnO/QD/CBP and glass/ZnO/QD structures are fabricated by the same methods as the QD-LEDs.

QD-LED Characterization: Current-density-voltage (J - V) characteristics are recorded in a nitrogen-filled glovebox using a computer-controlled Keithley 2636A current/voltage source meter. Simultaneously, front face EL power output through ITO is measured using a calibrated Newport 818-IR germanium photodiode and recorded with a computer-interfaced Newport Multi-Function Optical Meter 1835-C. The photodiode's active area is aligned with the emissive pixel and a diaphragm between the two prevents collection of waveguided EL from the glass substrate. Total radiated power (from which radiance-voltage (L - V) characteristics and power efficiency are obtained) is then calculated by assuming Lambertian emission and by accounting for the wavelength dependence (weighted by the device's EL spectrum) of the photodiode's responsivity (Section A, Supporting Information). EQE is calculated as the ratio of the number of forward-emitted photons to the number of injected electrons, per unit time (Section A, Supporting Information). Power conversion efficiency is defined as the radiated optical power divided by the input electrical power. For each QD type, L - J - V , and EQE data are taken from about three pixels per device, and from devices fabricated on two to five separate runs; the only exceptions are the “champion devices”, for which data comes from three to five pixels on one “champion” device (see Section A, Supporting Information). In all cases, variations between data for a given QD type are referred to as “device-to-device” variations in the text.

Optical Measurements: SWIR EL and PL spectra, transient PL data, and η_{PL} from the integrating sphere are collected in air, before which active sample areas are hermetically encapsulated by a glass coverslip in a nitrogen-filled glovebox using a solvent-free self-curing two-part epoxy (Torr Seal) rated to 10^{-9} Torr.

SWIR EL and steady-state PL data are collected through a $\lambda = 850$ nm long-pass filter with a Princeton Instruments Spectra Pro 300i spectrometer coupled to a liquid nitrogen-cooled Princeton Instruments OMA V InGaAs CCD array detector. The excitation source for steady-state SWIR PL is a $\lambda = 655$ nm diode laser (Thorlabs), which ensures that in the relative η_{PL} measurement only the QDs, and not ZnO or CBP, are significantly excited. The fixed geometry of the setup maximises the comparability of relative PL intensities. A fiber-coupled Ocean Optics SD2000 spectrometer is used to monitor for visible EL.

Transient PL data are measured by exciting glass/ZnO/QD samples at $\lambda = 633$ nm and collecting resulting PL using superconducting nanowire single-photon detectors, as previously reported.^[42]

For both steady-state and transient measurements of relative in situ QD η_{PL} , care was taken to record data in a low excitation-intensity regime (0.5 mW cm⁻² for the steady-state experiments) where PL intensity was not decaying with time (due to irreversible photobleaching), and at many sample locations to confirm homogeneity. To extract relative η_{PL} , steady-state PL spectra were scaled to account for the spectral responsivity of the InGaAs CCD and for differences in relative absorbance between QD samples. Absolute η_{PL} measurements are performed using an integrating sphere and calibrated reference detectors as described previously^[40] (Section D, Supporting Information).

SWIR EL photographs are taken with a Xenics Xeva-2.5–320 HgCdTe short-wave-infrared camera.

Supporting Information

Supporting Information is available from the Wiley Online Library or from the author.

Acknowledgements

The authors gratefully acknowledge technical assistance from Dr. Dong Kyun Ko, Dr. Gleb M. Akselrod, Dr. Danna Rosenberg, and Dr. Andrew J. Kerman. This work was supported in part by the U.S. Army Research Laboratory and the U.S. Army Research Office through the

Institute for Soldier Nanotechnologies, under Contract No. W911NF-13-D-0001. G.J.S., R.E.C., and Y.S. acknowledge support from the Center for Excitonics, an Energy Frontier Research Center funded by the U.S. Department of Energy (DOE), Office of Science, Basic Energy Sciences (BES), under Award No. DE-SC0001088. The authors also acknowledge the use of the facilities of the NSF MRSEC Center for Materials Science and of the MIT Electron Microprobe Facility. In part, this work is sponsored by the Assistant Secretary of Defense for Research and Engineering under Air Force Contract No. FA8721-05-C-0002. Opinions, interpretations, conclusions, and recommendations are those of the author and are not necessarily endorsed by the United States Government. K.W.S. acknowledges support from an NSF Graduate Research Fellowship. J.S. acknowledges Government support under FA9550-11-C-0028 and awarded by the Department of Defense, Air Force Office of Scientific Research, National Defense Science and Engineering Graduate (NDSEG) Fellowship, 32 CFR 168a.

Received: October 7, 2014

Revised: November 26, 2014

Published online: January 8, 2015

- [1] Y. Shirasaki, G. J. Supran, M. G. Bawendi, V. Bulović, *Nat. Photonics* **2013**, 7, 13.
- [2] L. Sun, J. J. Choi, D. Stachnik, A. C. Bartnik, B. R. Hyun, G. G. Malliaras, T. Hanrath, F. W. Wise, *Nat. Nanotechnol.* **2012**, 7, 369.
- [3] E. J. D. Klem, L. Levina, E. H. Sargent, *Appl. Phys. Lett.* **2005**, 87, 053101.
- [4] E. H. Sargent, *Adv. Mater.* **2005**, 17, 515.
- [5] J. V. Lim, Y. T. Kim, S. Nakayama, A. Stott, N. E. Bawendi, M. G. Frangioni, *Mol. Imaging* **2003**, 2, 50.
- [6] S. Kim, Y. T. Lim, E. G. Soltesz, A. M. De Grand, J. Lee, A. Nakayama, J. A. Parker, T. Mihaljevic, R. G. Laurence, D. M. Dor, L. H. Cohn, M. G. Bawendi, J. V. Frangioni, *Nat. Biotechnol.* **2004**, 22, 93.
- [7] I. L. Medintz, H. T. Uyeda, E. R. Goldman, H. Mattoussi, *Nat. Mater.* **2005**, 4, 435.
- [8] M. F. Frasco, N. Chaniotakis, *Sensors* **2009**, 9, 7266.
- [9] G. Qian, Z. Zhong, M. Luo, D. Yu, Z. Zhang, Z. Y. Wang, D. Ma, *Adv. Mater.* **2009**, 21, 111.
- [10] O. Chen, J. Zhao, V. P. Chauhan, J. Cui, C. Wong, D. K. Harris, H. Wei, H.-S. Han, D. Fukumura, R. K. Jain, M. G. Bawendi, *Nat. Mater.* **2013**, 12, 1.
- [11] K. S. Cho, E. K. Lee, W. Joo, E. Jang, T. Kim, S. J. Lee, S. Kwon, J. Y. Han, B. Kim, B. L. Choi, J. M. Kim, *Nat. Photonics* **2009**, 3, 341.
- [12] K. Y. Cheng, R. Anthony, U. R. Kortshagen, R. J. Holmes, *Nano Lett.* **2011**, 11, 1952.
- [13] C. Borek, K. Hanson, P. I. Djurovich, M. E. Thompson, K. Aznavour, R. Bau, Y. Sun, S. R. Forrest, J. Brooks, L. Michalski, J. Brown, *Angew. Chem.* **2007**, 46, 1109.
- [14] X. Dai, Z. Zhang, Y. Jin, Y. Niu, H. Cao, X. Liang, L. Chen, J. Wang, X. Peng, *Nature* **2014**, 515, 96.
- [15] M. C. Schlamp, X. Peng, A. P. Alivisatos, *J. Appl. Phys.* **1997**, 82, 5837.
- [16] B. N. Pal, Y. Ghosh, S. Brovelli, R. Laocharoensuk, V. I. Klimov, J. A. Hollingsworth, H. Htoon, *Nano Lett.* **2012**, 12, 331.
- [17] N. Tessler, V. Medvedev, M. Kazes, S. Kan, U. Banin, *Science* **2002**, 295, 1506.
- [18] O. Solomeshch, A. Kigel, A. Saschiuk, V. Medvedev, A. Aharoni, A. Razin, Y. Eichen, U. Banin, E. Lifshitz, N. Tessler, *J. Appl. Phys.* **2005**, 98, 074310.
- [19] P. Moroz, G. Liyanage, N. N. Kholmicheva, S. Yakunin, U. Rijal, P. Uprety, E. Bastola, B. Mellott, K. Subedi, L. Sun, M. V. Kovalenko, M. Zamkov, *Chem. Mater.* **2014**, 26, 4256.
- [20] J. M. Pietryga, D. J. Werder, D. J. Williams, J. L. Casson, R. D. Schaller, V. I. Klimov, J. A. Hollingsworth, *J. Am. Chem. Soc.* **2008**, 130, 4879.
- [21] Z. B. Wang, M. G. Helander, J. Qiu, Z. W. Liu, M. T. Greiner, Z. H. Lu, *J. Appl. Phys.* **2010**, 108, 024510.
- [22] Z. B. Wang, M. G. Helander, J. Qiu, D. P. Puzzo, M. T. Greiner, Z. M. Hudson, S. Wang, Z. W. Liu, Z. H. Lu, *Nat. Photonics* **2011**, 5, 753.
- [23] R. A. M. Hikmet, D. V. Talapin, H. Weller, *J. Appl. Phys.* **2003**, 93, 3509.
- [24] Catalogue of commercially available IR LEDs from a commercial supplier, www.roithner-laser.com (accessed December 2014).
- [25] J. M. Caruge, J. E. Halpert, V. Wood, V. Bulović, M. G. Bawendi, *Nat. Photonics* **2008**, 2, 247.
- [26] P. P. Jha, P. Guyot-Sionnest, *J. Phys. Chem. C* **2010**, 114, 21138.
- [27] R. Change, R. R. Prock, A. Silbey, in *Adv. Chem. Phys.* (Eds: S. A. Prigogine, I. Rice), John Wiley & Sons, Inc., New York **1978**, Vol. 37, pp. 1–65.
- [28] P. R. Brown, R. R. Lunt, N. Zhao, T. P. Osedach, D. D. Wanger, L. Y. Chang, M. G. Bawendi, V. Bulović, *Nano Lett.* **2011**, 11, 2955.
- [29] F. W. Wise, J. D. Goodreau, J. R. Matthews, T. M. Leslie, N. F. Borrelli, *ACS Nano* **2008**, 2, 2206.
- [30] K. Tvrđy, P. A. Frantsuzov, P. V. Kamat, *Proc. Natl. Acad. Sci. USA* **2011**, 108, 29.
- [31] N. Song, H. Zhu, Z. Liu, Z. Huang, D. Wu, T. Lian, *ACS Nano* **2013**, 7, 1599.
- [32] H. C. Leventis, F. O'Mahony, J. Akhtar, M. Afzaal, P. O'Brien, S. A. Haque, *J. Am. Chem. Soc.* **2010**, 132, 2743.
- [33] B. R. Fisher, H. J. Eisler, N. E. Stott, M. G. Bawendi, *J. Phys. Chem. B* **2004**, 108, 143.
- [34] M. Jun Mei, S. Bradley, V. Bulović, *Phys. Rev. B* **2009**, 79, 235205.
- [35] R. Buonsanti, A. Llordes, S. Aloni, B. A. Helms, D. J. Milliron, *Nano Lett.* **2011**, 11, 4706.
- [36] J. F. Znaidi, L. Benyahia, S. Marchand, C. Gaston, J. P. Kurdi, J. Guillemoles, *Proc. 19th European Photovoltaic Solar Energy Conf. (Paris)*, ETA-Florence, Italy & WIP-Munich, Germany, **2004**, 1, 301.
- [37] W. K. Bae, Y.-S. Park, J. Lim, D. Lee, L. A. Padilha, H. McDaniel, I. Robel, C. Lee, J. M. Pietryga, V. I. Klimov, *Nat. Commun.* **2013**, 4, 2661.
- [38] B. S. Mashford, M. Stevenson, Z. Popovic, C. Hamilton, Z. Zhou, C. Breen, J. Steckel, V. Bulović, M. Bawendi, S. Coe-Sullivan, P. T. Kazlas, *Nat. Photonics* **2013**, 7, 407.
- [39] V. Wood, M. J. Panzer, J. E. Halpert, J. M. Caruge, M. G. Bawendi, V. Bulović, *ACS Nano* **2009**, 3, 3581.
- [40] M. A. Hines, G. D. Scholes, *Adv. Mater.* **2003**, 15, 1844.
- [41] M. V. Kovalenko, R. D. Schaller, D. Jarzab, M. A. Loi, D. V. Talapin, *J. Am. Chem. Soc.* **2012**, 134, 2457.
- [42] R. E. Correa, E. A. Dauler, G. Nair, S. H. Pan, D. Rosenberg, A. J. Kerman, R. J. Molnar, X. Hu, F. Marsili, V. Anant, K. K. Berggren, M. G. Bawendi, *Nano Lett.* **2012**, 12, 2953.
- [43] S. M. Geyer, J. M. Scherer, N. Moloto, F. B. Jaworski, M. G. Bawendi, *ACS Nano* **2011**, 5, 5566.
- [44] M. G. Helander, Z. B. Wang, J. Qiu, M. T. Greiner, D. P. Puzzo, Z. W. Liu, Z. H. Lu, *Science* **2011**, 332, 944.
- [45] Y. Sun, J. H. Seo, C. J. Takacs, J. Seifert, A. J. Heeger, *Adv. Mater.* **2011**, 23, 1679.
- [46] H. Lee, H. C. Leventis, S. J. Moon, P. Chen, S. Ito, S. A. Haque, T. Torres, F. Nüesch, T. Geiger, S. M. Zaakeeruddin, M. Grätzel, M. K. Nazeeruddin, *Adv. Funct. Mater.* **2009**, 19, 2735.
- [47] J. Jasieniak, M. Califano, S. E. Watkins, *ACS Nano* **2011**, 5, 5888.
- [48] M. T. Greiner, M. G. Helander, W.-M. Tang, Z.-B. Wang, J. Qiu, Z. H. Lu, *Nat. Mater.* **2012**, 11, 76.
- [49] Y. Park, V. Choong, Y. Gao, B. R. Hsieh, C. W. Tang, *Appl. Phys. Lett.* **1996**, 68, 2699.